Article

Not peer-reviewed version

A Small Power Margin and Bandwidth Expansion Allow Data Transmission During Rainfall Despite Large Attenuation: Application to GeoSurf Satellite Constellations at mm–Waves

Emilio Matricciani *

Posted Date: 1 March 2024

doi: 10.20944/preprints202403.0017.v1

Keywords: bandwidth expansion; GeoSurf; link efficiency; power margin; rain attenuation; satellite constellation Synthetic Storm Technique

 doi:10.20944/preprints202403.0017.v1

Article

A Small Power Margin and Bandwidth Expansion Allow Data Transmission During Rainfall Despite Large Attenuation: Application to GeoSurf Satellite Constellations at mm–Waves

Emilio Matricciani

The Dipartimento di Elettronica, Informazione e Bioingegneria (DEIB), Politecnico di Milano, Milan, Italy; emilio.matricciani@polimi.it

Abstract: The traditional approach of considering the probability distribution of rain attenuation leads to overdesign the power margin of data channels. We have first recalled a method, proposed in 2016, which with a small power margin, bandwidth expansion and variable symbol rate avoids overdesign and can transfer the same data volume as if the link were in clear–sky conditions. It is charaterized only by the link mean efficiency $0 \leq \eta \leq 1$, suitably defined. It is usefull only if: (a) data must be downloaded also when it is raining; (b) real–time communication is not strictly required. We have applied it to the links of GeoSurf satellite constellations by simulating rain attenuation time series at 80 GHz (mm–wave) with the Synthetic Storm Technique, from rain-rate time series recorded on–site, at sites located in different climatic regions. The power margin to be implemented ranges from 2.0 dB to 7.4 dB – well within the current technology – regardless the instantaneous rain attenuation. The clear–sky bandwidth is expanded 1.75 to 2.80 times, not large *per se*, but it may challenge current technology if the clear–sky bandwidth is already large.

Keywords: bandwidth expansion; GeoSurf; link efficiency; power margin; rain attenuation; satellite constellation Synthetic Storm Technique

1. Introduction

In designing satellite links above 10 GHz – frequency beyond which the attenuation due to rainfall is no longer neglible – the traditional approach is to consider the average (annual or worst month) probability distribution $P(A)$ of exceeding rain attenuation A (dB) [1–9]. In the design, $P(A)$ is considered the outage probability and A (dB) the required power margin necessary to maintain the link working, i.e. delivering data with the mininum tolerated probability of symbol error. In [10], we have shown that in data channels this approach is too pessimistic and leads to large overdesign.

If the data volume downloadable during rainfall, with a constant probability of symbol error, is more valuable than the instantaneous symbol rate – e.g. in remote sensing and internet of things (IoT) using satellites – the method discussed in [10] can avoid overdesign. This method is usefull when: (a) data must be downloaded also when it is raining (e.g., because of satellite pass, or other technical or service constraints); (b) real–time communication is not strictly required.

The method is charaterized only by a single parameter, namely the mean efficiency $0 \leq \eta \leq 1$ of the link, suitably defined in [10] and recalled in Section 2. Theoretically, the method can achieve the same data volume down-loaded/up-loaded as if the link were in clear–sky conditions, and is directly applicable to QPSK, M–PSK and implements [10] Shannon's channel capacity.

In synthesis, according to the theory, a small power margin – regardless of instantaneous rain attenuation – and a small bandwidth expansion allow to deliver an average symbol rate equal to the symbol rate obtainable when $A = 0$, therefore down-loading/up-loading the same data volume in the same interval, as if there were no rainfall. In [10] we have compared its theoretical performance with the Adaptive Coding and Modulation (ACM) techniques [11–13] and shown that, even theoretically,

 doi:10.20944/preprints202403.0017.v1

these latter cannot achieve the maximum efficiency [14–19] as, on the contrary, the method theoretically does.

In the present paper, we apply the method to the links of GeoSurf satellite constellations [20]. These constellations share most advantages of GEO (Geostationary), MEO (Medium Earth Orbit) and LEO (Low Earth Orbit) satellite constellations, without suffering many of their drawbacks (see Table 1 of [20]) because the propagation paths are vertical (at the local zenith) at any latitude.

No measurements or predictions are, however, available for zenith paths, therefore we consider as experimental results the rain attenuation time series $A(t)$ simulated in zenith paths with the Synthetic Storm Technique (SST) (see Equation (29) of [21], or [3]) from rain-rate time series $R(t)$, recorded on–site for several years in the sites listed in Table 1. The SST is a powerful tool [2-5; 22-28].

The sites are in different climatic regions; therefore, the findings show how the design would change worldwide. Moreover, these particular sites are important study–cases because satellite ground stations of NASA and ESA are located there (Fucino, Madrid, White Sands), or because long–term radio propagation experiments were performed at the sites (Fucino, Gera Lario, Madrid, Spino d'Adda), or just because there are large cities (Prague, Norman, Tampa, Vancouver). Following our previous studies of the GeoSurf links [2–5,28], we simulate $A(t)$ at 80 GHz (mm–wave), circular polarization.

After this introduction, in Section 2 we summarize the theory of the method mentioned above; in Section 3 we calculate link efficiency – and related parameters – in the zenith paths at the sites indicated in Table 1; in Section 4 we extend the theory by considering extra fixed power margins; in Section 5 we summarize and discuss the main findings and indicate future work.

Table 1. Geographical coordinates, altitude (km), number of years of continuous rain-rate time series measurements at the indicated sites.

Site	Latitude N (°)	Longitude E (°)	Altitude H_S (m)	Rain Rate Observation Time (Years)
Spino d'Adda (Italy)	45.4	9.5	84	8
Gera Lario (Italy)	46.2	9.4	210	5
Fucino (Italy)	42.0	13.6	680	5
Madrid (Spain)	40.4	356.3	630	8
Prague (Czech Republic)	50.0	14.5	250	5
Tampa (Florida)	28.1	277.6	50	4
Norman (Oklahoma)	35.2	262.6	420	4
White Sands (New Mexico)	32.5	253.4	1463	5
Vancouver (British Columbia)	49.2	236.8	80	3

2. The Method to Download Clear–Sky Data Volume during Rainfall

We briefly recall the theory of the method developed in [10]. We first define the channel efficiency $\boldsymbol{\eta}$ and then we use this parameter to determine the power margin and the bandwidth expansion necessary for designing a channel that delivers the same data volume as if there were no rainfall.

2.1. Channel Efficiency

To deliver a fixed signal–to–noise ratio ρ_o in BPSK and QPSK modulation schemes, standard calculations show that, the instantaneous symbol rate $R_s(t)$ (symbols per second) at time t, with rain attenuation $A(t)$, must be [10]:

$$R_s(t) \geq \frac{P_r \times 10^{-A_G/10} \times 10^{-A(t)/10}}{k(T_m + T_{rec})\rho_o} = R_o \times 10^{-A(t)/10} \quad (1)$$

 doi:10.20944/preprints202403.0017.v1

$$R_o = \frac{P_r \times 10^{-A_G/10}}{k(T_m + T_{rec})\rho_o} \quad (2)$$

In Equations (1)(2) T_m(K) is the mean physical raindrops temperature (supposed to be constant), T_{rec}((K) is the receiver equivalent noise temperature; A_G(dB) is the total attenuation due to water vapor, oxygen, clouds, supposed to be constant during rainfall (this restriction can be removed, see below); $\rho_o = E_b/N_o$ is the signal–to–noise ratio tolerated, E_b is the received energy per symbol, $N_o = k(T_m + T_{rec})$ is the one–sided noise power spectral density.

The inequality (1) arises because the antenna noise temperature $T_{sky} \leq T_m$ (K) is, in fact, upper bounded by T_m, a conservative hypothesis that models rain fade – for noise calculation – as due to a passive attenuator at physical temperature T_m with $A \to \infty$ [29]. We do not consider scintillation because this phenomenon is negligible in implementing the method [10].

In [10] we studied Equation (1) under the hypothesis of providing the minimum equivalent and tolerable ρ_o (fixed by the tolerated maximum probability of symbol error) by reducing $R_s(t)$. In other words, the channel must match dynamically $R_s(t)$ to the slow (compared to $R_s(t)$) time–varying $A(t)$. Therefore, the volume of symbols downloaded during the rain attenuation time T_A is given by:

$$D = \int_0^{T_A} R_s(t)dt = R_o \int_0^{T_A} 10^{-A(t)/10}dt = R_o\tau \quad (3)$$

$$\tau = \int_0^{T_A} 10^{-A(t)/10}dt \quad (4)$$

The integral in Equation (4) gives the equivalent time τ during which the constant rate R_o delivers the same total data volume D. In other words, the perfect matching (1) in the interval T_A is equivalent to transmitting the symbol rate R_o in an ideal channel with $A(t) = 0$ dB, but for the shorter equivalent interval τ. This finding applies also M–PSK modulation and to Shannon's capacity formula [10].

The mean channel efficiency η is defined as:

$$\eta = \frac{1}{T_A}\int_0^{T_A} 10^{-A(t)/10}dt = \frac{\tau}{T_A} \quad (5)$$

Of course, $0 \leq \eta \leq 1$ because if $A \to \infty$ then $\tau = 0$, $\eta = 0$; if $A = 0$ (no rainfall) then $\tau = T_A$, $\eta = 1$.

Notice that it is not necessary to consider rain–attenuation time series $A(t)$ but only the conditional complementary long–term probability distribution $P_c(A) = P(A)/P_o$, with $P_o = P(A > 0) = T_A/T_{obs}$ where $T_{obs} \geq T_A$ is the observation time (a year, a moth, etc.). It can be shown [10] that:

$$\eta = 1 - \frac{\ln(10)}{10}\int_0^{\infty} 10^{-A/10}P_c(A)dA \quad (6)$$

Notice that a fixed power margin $S > 0$ (dB) – see Section 4 below –, gain (site diversity, time diversity etc.) or a constant fade can be introduced in Equation (1) by only changing R_o, not the mean efficiency (5)(6). This argument applies also to a constant interference power, if we consider it another source of Gaussian noise (worst case, according to Shannon). In other words, all constant parameters do change R_o but not η.

The mean efficiency (6) is a random variable bounded in a range calculated by applying the Cauchy–Schwarz inequality [10]:

$$\left[1 - \frac{\ln(10)}{20}\int_0^{\infty} 10^{-A/20}P_c(A)dA\right]^2 \leq \eta \leq \sqrt{1 - \frac{\ln(10)}{5}\int_0^{\infty} 10^{-A/5}P_c(A)dA} \quad (7)$$

2.2. Power Margin and Bandwidth Expansion

The concept of mean efficiency is at the foundation of the method [10]. If it could be perfectly implemented, the mean symbol rate in the interval T_A, and hence also in the observation period T_{obs}, would be equal to the symbol rate obtainable when $A = 0$, therefore restoring the full data volume

 doi:10.20944/preprints202403.0017.v1

down–loaded/up–loaded. As we have shown in [10], the cost to pay is only a small increase in the transmitted power and a relatively small expansion of the bandwidth, the latter a less intuitive fact.

Let us introduce in (1) a fixed power margin $1/\eta \geq 1$, so that the received power is:

$$P_{r,\eta} = P_r/\eta \tag{8}$$

This power can deliver a constant ρ_o only if the instantaneous symbol rate is:

$$R_S^*(t) = (R_o/\eta) \times 10^{-A(t)/10} \tag{9}$$

The ratio, $\gamma(t)$, between the symbol rate $R_s^*(t)$ and R_o is given by:

$$\gamma(t) = \frac{R_s^*(t)}{R_o} = \frac{1}{\eta} \times 10^{-A(t)/10} \tag{10}$$

According to Equation (9), the bandwidth is multiplied by $1/\eta$ when $A(t) \to 0$, i.e. at the beginning and at the end of rainfall. This is the maximum bandwidth required. For example, assuming a QPSK modulation scheme [10], the radiofrequency bandwidth is $B_{RF}^* = (1+\delta)R_S^*(t)/2$, therefore, $B_{RF}^* \leq (1+\delta)R_o/(2\eta)$, the equality sign holding when $A(t) \to 0$. Moreover, compared to the bandwidth of QPSK in clear–sky conditions $B_{RF,CS} = (1+\delta)R_o/2, \leq (1+\delta)R_o/(2\eta)$, with the equality sign holding, of course, only if $\eta = 1$, i.e. no rainfall.

In other words, as soon as $A(t) = 0^+$, power and symbol rate are both simultaneously increased according to Equations (8) and (9), being the latter increase counterintuitive. For example, if $\eta = 0.5$, then at $t = 0^+$ $P_{r,\eta} = 2P_r$ and the symbol rate starts with the maximum value required $R_S^*(0) = 2R_o$ (and maximum bandwidth), which decreases according to Equation (9).

In conclusion, by using the fixed power margin M (dB):

$$M = -10 \times \log_{10}\eta \tag{11}$$

and a maximum bandwidth expansion factor:

$$W = 1/\eta \tag{12}$$

the total data volume would be equal to that downloaded in clear–sky conditions in the same interval T_A.

In the next sections we apply these concepts to rain attenuation at 80 GHz, circular polarization, simulated with the SST in zenith paths at the sites listed in Table 1.

3. Link Efficiency in Zenith Paths

We first show the findings on the mean efficiency and secondly its application to examples of rain attenuation time series $A(t)$ at the sites of Table 1.

3.1. Probability Distributions $P(R)$, $P(A)$ and Channel Efficiency

Figure 1 shows the average annual probability distribution $P(R)$ of exceeding R (mm/h, averaged in 1 min) at the indicated sites. The different climatic conditions of these sites are clearly evident by comparing the rain rate exceeded with the same probability.

Figure 2 shows the average annual probability distribution $P(A)$ of exceeding A (dB) in the zeith paths at the indicated sites, simulated with SST (see Eq. (29) of [21] and [3]). These probability distributions are the data necessary to calculate the mean efficiency and its bounds (Equations (6), (7)), the power margin (Equation (11)) and the bandwidth expansion factor (Equation (12)).

Table 2 reports the mean and minimum (worst case) efficiency. The mean efficiency ranges from 0.265 at Tampa ("worst" site) to 0.502 at Fucino ("best" site), consequently the power margins – reported in Table 3 – and the bandwidth expansion factor – Table 4 – are, respectively 5.76 dB and 3.77 at Tampa, 2.99 dB and 1.99 at Fucino.

Preprints.org (www.preprints.org) | NOT PEER-REVIEWED | Posted: 1 March 2024 doi:10.20944/preprints202403.0017.v1

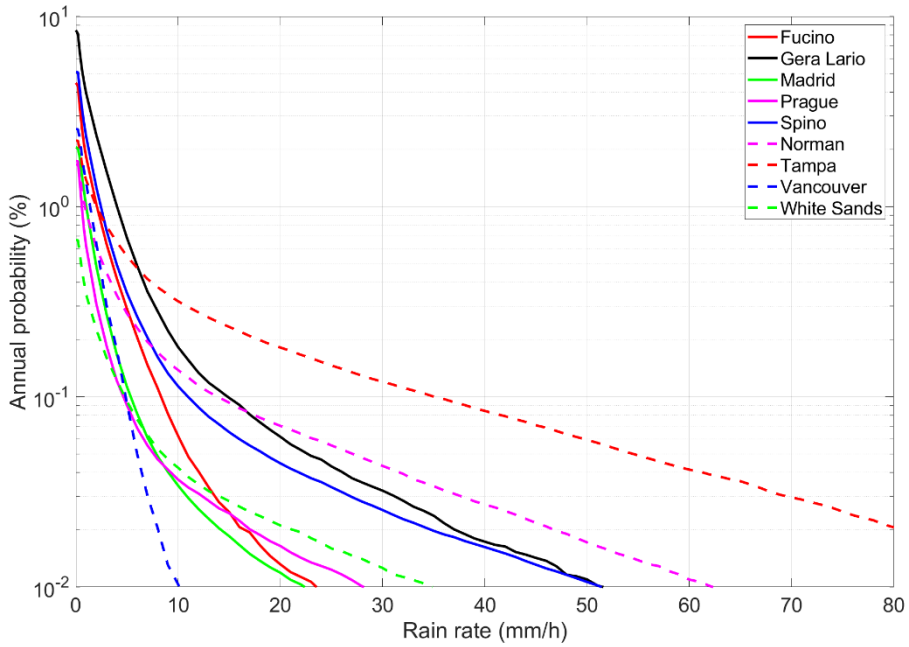

Figure 1. Annual probability distribution (%) $P(R)$ of exceeding the value indicated in abscissa at the indicated sites. Spino d'Adda: continuous blue line; Gera Lario: continuous black line; Fucino: continuous red line; Madrid: continuous green line; Prague: continuous magenta line; Tampa: dashed red line; Norman: dashed magenta line; White Sands: dashed green line; Vancouver: dashed blue line.

The power margins are always small, well within current technology. The bandwidth expansion factors might be large if the bandwidth in clear–sky conditions is already large; therefore, this might be the most critical issue in practical applications of the method. The evolution of spread–spectrum technology could ease its application [30–34].

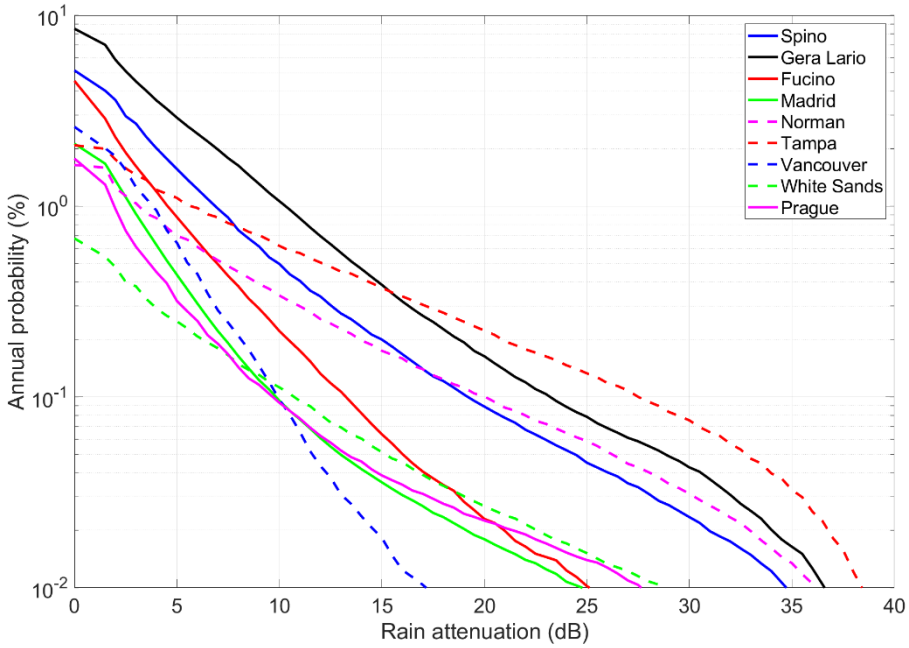

Figure 2. Annual probability distribution (%) $P(A)$ of exceeding the value indicated in abscissa–80 GHz, circular polarization, zenith paths–at the indicated sites. Spino d'Adda: continuous blue line; Gera Lario: continuous black line; Fucino: continuous red line; Madrid: continuous green line; Prague: continuous magenta line; Tampa: dashed red line; Norman: dashed magenta line; White Sands: dashed green line; Vancouver: dashed blue line.

 doi:10.20944/preprints202403.0017.v1

Table 2. Minimum (worst case) and mean values of channel efficiency η, Equations (6)(7), in zenith links working at 80 GHz at the indicated sites.

Site	Minimum	Mean
Spino d'Adda (Italy)	0.378	0.403
Gera Lario (Italy)	0.358	0.386
Fucino (Italy)	0.483	0.502
Madrid (Spain)	0.444	0.458
Prague (Czech Republic)	0.473	0.492
Tampa (Florida)	0.221	0.265
Norman (Oklahoma)	0.282	0.318
White Sands (New Mexico)	0.338	0.377
Vancouver (British Columbia)	0.421	0.431

Table 3. Maximum (worst case) and mean value of channel power margin factor M, (dB), Equation (11), in zenith links working at 80 GHz at the indicated sites.

Site	Maximum	Mean
Spino d'Adda (Italy)	4.21	3.95
Gera Lario (Italy)	4.46	4.13
Fucino (Italy)	3.16	2.99
Madrid (Spain)	3.53	3.39
Prague (Czech Republic)	3.25	3.08
Tampa (Florida)	6.56	5.76
Norman (Oklahoma)	5.50	4.97
White Sands (New Mexico)	4.71	4.24
Vancouver (British Columbia)	3.76	3.66

Table 4. Maximum (worst case, corresponding to minimum efficiency of Table 2) and mean value of bandwidth expansion factor W, Equation (12), in zenith links working at 80 GHz at the indicated sites.

Site	Maximum	Mean
Spino d'Adda (Italy)	2.64	2.48
Gera Lario (Italy)	2.80	2.59
Fucino (Italy)	2.07	1.99
Madrid (Spain)	2.25	2.18
Prague (Czech Republic)	2.11	2.03
Tampa (Florida)	4.53	3.77
Norman (Oklahoma)	3.55	3.14
White Sands (New Mexico)	2.96	2.66
Vancouver (British Columbia)	2.38	2.32

Finally, notice that the different meteorological conditions of the sites (see Figures 1, 2) lead to different efficiency.

Preprints.org (www.preprints.org) | NOT PEER-REVIEWED | Posted: 1 March 2024 doi:10.20944/preprints202403.0017.v1

3.2. Examples of Theoretical Application to Time Series $A(t)$

To grasp the time evolution of the symbol rate during a rain attenuation event, Figures 3, 4 show examples of $A(t)$ and $\gamma(t)$, Equation (10), simulated at Spino d'Adda and at Tampa, by adopting the mean efficiency (Table 2). Appendix A reports similar examples for the other sites.

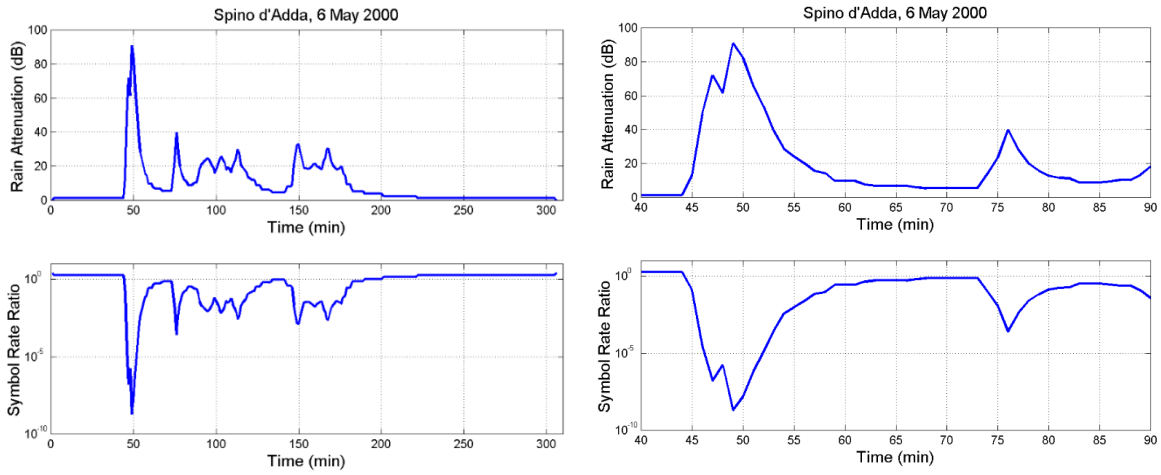

(**a**) (**b**)

Figure 3. Upper Panel: (a) Rain attenuation time series $A(t)$: (b) detail. **Lower panel**: (a) Symbol rate ratio $\gamma(t)$; (b) detail. Spino d'Adda.

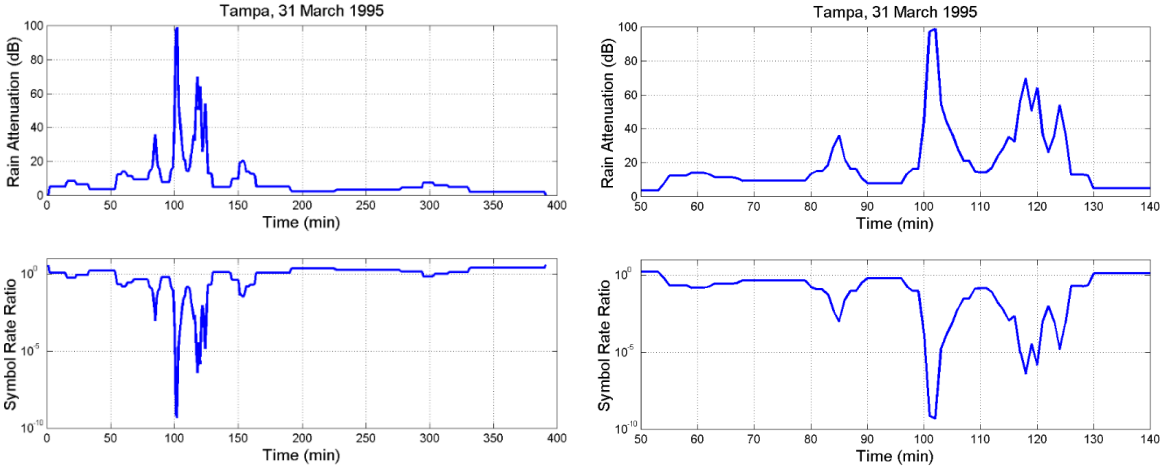

(**a**) (**b**)

Figure 4. Upper Panel: (a) Rain attenuation time series $A(t)$: (b) detail. **Lower panel**: (a) Symbol rate ratio $\gamma(t)$; (b) detail. Tampa.

With straight calculations we can realize the quantities involved in implementing the method. At Spino d'Adda $\gamma = 2.48$ at the beginning of the event, i.e. when $A(t) = 0$ (Table 4) and $\gamma = 1.97 \times 10^{-9}$ at the peak $A = 91.0$ dB (Figure 3). Therefore, for example, if $R_o = 5 \times 10^9$ symbols per second, then for long intervals (Figure 3, low attenuation range) the symbol rate would increase to $R_s^* = 2.48 \times 5 \times 10^9 = 12.40 \times 10^9$ symbols per second. Then it would decrease smoothly from this value – according to $A(t)$ – to reach the minimum value $R_s^* = 1.97 \times 10^{-9} \times 5 \times 10^9 \approx 10$ symbols per second at the attenuation peak. This very large range gives a clear indication on the technological issues involved in changing symbol rate and bandwidth. However, the method promises to avoid the large power margin required for a continuous transmission– up to the fantastic value 91.0 dB – in conventional design.

In Figures 3, 4 it is interesting to notice – also in those reported in Appendix A – that, regardless of the site, the interval of the onset of a peak is smaller than that of its decay, i.e. the two time-constants

Preprints.org (www.preprints.org) | NOT PEER-REVIEWED | Posted: 1 March 2024 doi:10.20944/preprints202403.0017.v1

are signficantly diverse. For example, in Figure 3 (Spino d'Adda) $A(t)$ increases from 13.2 dB to the peak 91.0 dB in 5 minutes while it decreases to 14.5 dB in 9 minutes, i.e. with rate of change $+15.6$ dB per minute and -8.5 dB per minute, respectively. Similar observations can be done for the evolution of the ratio $\gamma(t)$. For Tampa, $A(t)$ increases from 13.3 dB to the peak 98.9 dB in 5 minutes while it decreases to 14.3 dB in 9 minutes, i.e. with rate of change $+17.2$ dB per minute and -9.5 dB per minute, respectively.

In other words, the intense rainfall causing attenuation peaks fades away slower at its end than at its onset, therefore, the long time–scale (several minutes) positive rates of change of attenuation are larger than the negative ones. This behavior at zenith paths is significantly different of that occurring in slant paths for which the magnitude of positive and negative rates of change are statistical identical, according to the experimental results [35–40] and modeling [41].

In the next section we consider an evolution of the method by assuming that it is applied in links in which a power margin is already implemented. We show next that this fixed power margin is very low small.

4. Design with Extra Fixed Power Margin

In Section 3 the method is implemented at the onset of rainfall. In this section we suppose that a power margin S (dB) is already implemented in the link so that the method is applied only in the intervals in which the attenuation threshold S is exceeded, i.e. when $A(t) \geq S \geq 0$. The theory recalled in Section 2 can be fully applied to this case by considering, now, the variable $A^*(t) = A(t) - S$ and applying Equations (8)-(12) to the conditional probability distribution $P_c(A^*) = P(A^*)/P_o^*$ in which $P_o^* = P(S)$, all calculated from the data drawn in Figure 2. Of course, if $S = 0$, we obtain the results of Section 3.

Figure 5 shows mean and bounds of the efficiency versus S, at Spino d'Adda. Figure 6 shows the corresponding values of the extra power margin, Figure 7 shows the corresponding values of the bandwidhth expansion factor. Similar curves are obtained for the other sites (not shown for brevity).

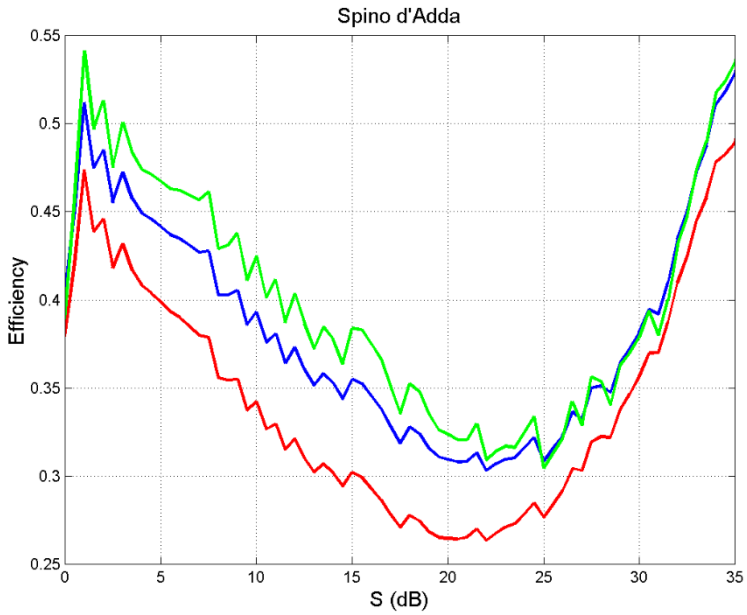

Figure 5. Mean (blue line) and upper (green line), lower (red line) bounds of the efficiency η versus the threshold S, at Spino d'Adda.

Preprints.org (www.preprints.org) | NOT PEER-REVIEWED | Posted: 1 March 2024 doi:10.20944/preprints202403.0017.v1

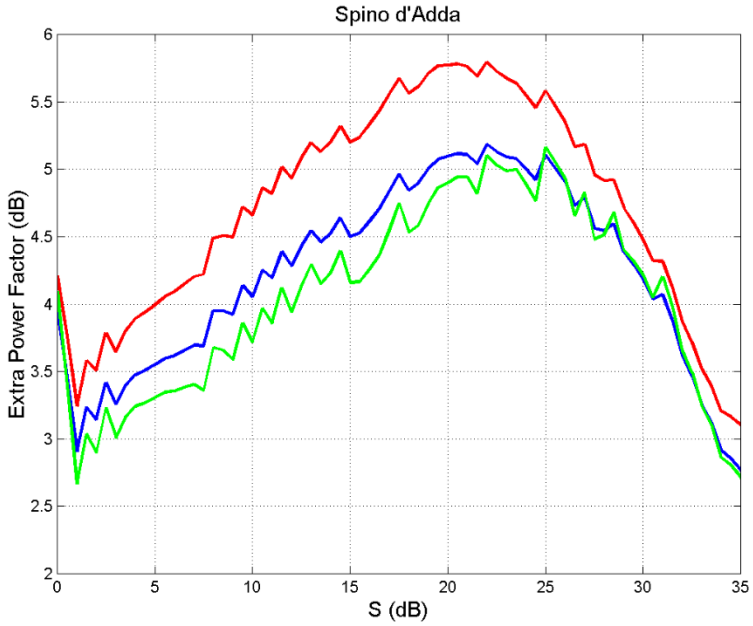

Figure 6. Extra power factor given by the mean (blue line), upper (green line) and lower (red line) bounds of the efficiency, versus the threshold S, at Spino d'Adda.

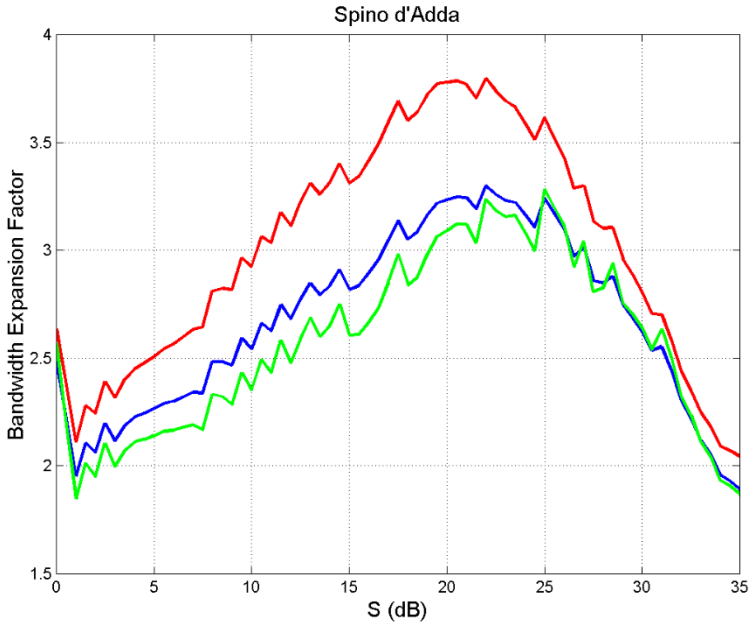

Figure 7. Maximum bandwidth expansion factor given by the mean (blue line), upper (green line) and lower (red line) bounds of the efficiency, versus the threshold S, at Spino d'Adda.

Figures (8)(9) show the curves obtained for all sites by considering only the mean efficiency. We can notice trends very similar to those of Spino d'Adda, therefore confirming a general behavior of efficiency, and its related parameters, versus S. However, differences from site to site are clearly evident, Tampa being the "worst" site.

Preprints.org (www.preprints.org) | NOT PEER-REVIEWED | Posted: 1 March 2024 doi:10.20944/preprints202403.0017.v1

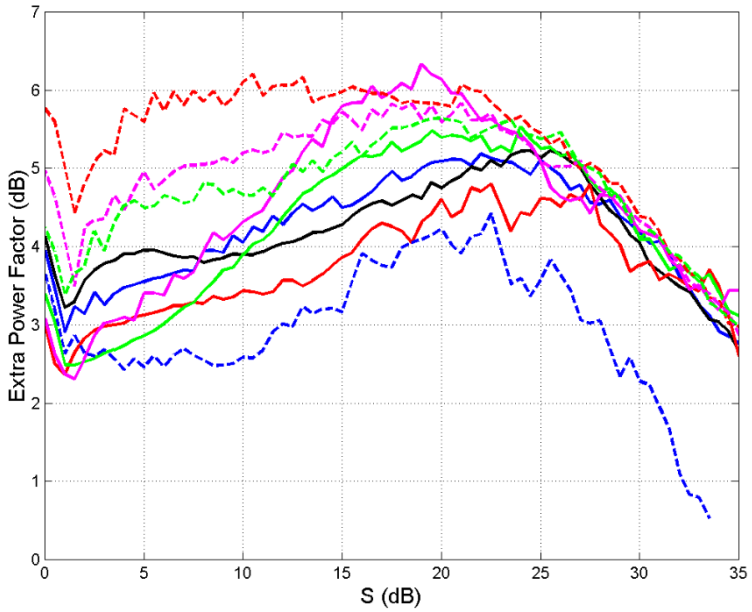

Figure 8. Extra power factor given by the mean (blue line), upper (green line) and lower (red line) bounds of the efficiency, versus the threshold S, at the indicated sites. Spino d'Adda: continuous blue line; Gera Lario: continuous black line; Fucino: continuous red line; Madrid: continuous green line; Prague: continuous magenta line; Tampa: dashed red line; Norman: dashed magenta line; White Sands: dashed green line; Vancouver: dashed blue line.

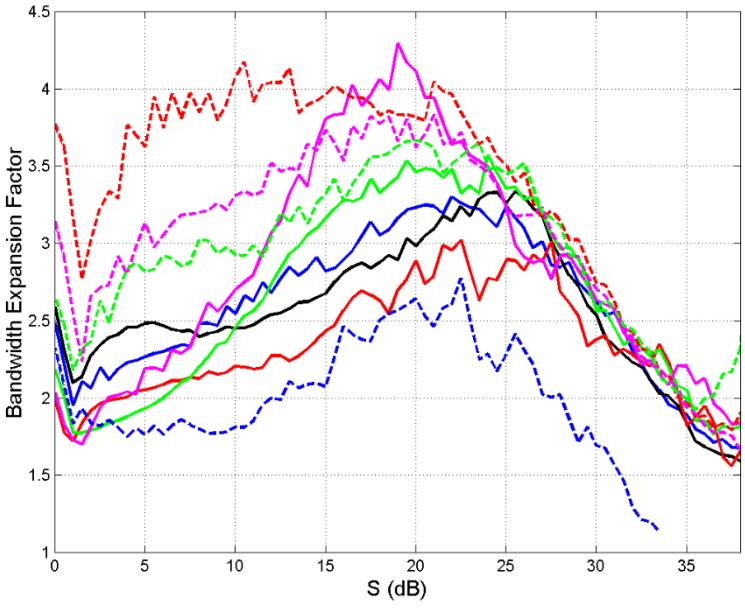

Figure 9. Maximum bandwith expansion factor given by the mean (blue line), upper (green line) and lower (red line) bounds of the efficiency, versus the threshold S, at the indicated sites. Spino d'Adda: continuous blue line; Gera Lario: continuous black line; Fucino: continuous red line; Madrid: continuous green line; Prague: continuous magenta line; Tampa: dashed red line; Norman: dashed magenta line; White Sands: dashed green line; Vancouver: dashed blue line.

From these figures concerning Spino d'Adda we can observe the following interesting findings, applicable also to all sites:

(a) The efficiency is maximum at lower thresholds, but not at $S = 0$ dB.

Preprints.org (www.preprints.org) | NOT PEER-REVIEWED | Posted: 1 March 2024 doi:10.20944/preprints202403.0017.v1

(b) The extra power margin is minimum in according with efficiency.
(c) The bandwidth expansion factor is minimum in according with efficiency.
(d) The efficiency is minimum (worst case) at about $S \approx 20$ dB.
(e) For $S >\gtrsim 20$ dB another maximum efficiency occurs, but this range is not attractive because of the very large power margin.

Figure 10 shows details at the low threshold range, which suggests an optimum use of the method. Here, it is interesting to notice that there is no sensible difference in the extra power factor (left panel) in the range $0 \leq S \lesssim 1.5$ dB (right panel), while minima are clearly evident in the bandwidth expansion factor in the ranget $S \approx 0.5\sim1.5$ dB. In other words, at any site, the method can be applied when $A(t) \gtrsim 0.5\sim1.5$ dB, therefore a power margin $0.5\sim1.5$ dB should be provided before applying the method. For example, for Tampa geographical area (worst site) the final total power margin necessary would be $1.5 + 5.9 = 7.4$ dB, with a bandwidth expansion factor ≈ 2.8, being $S = 1.5$ dB the threshold of minimum bandwidth expansion factor (Figure 10, right panel) and ~ 5.9 dB the extra power factor (Figure 10, left panel).

Table 5 reports these optimum values for all sites. The total power margin ranges from 2.0 dB (Norman) to 7.4 dB (Tampa) and the bandwidth expansion factor ranges from 1.70 (Prague) to 2.80 (Tampa). As already observed, the power margin required is very small for all sites, well within the current technology. The bandwith expansion factor *per se* is not very large, but it can be relatively large if the clear–sky bandwidth is already large for the current technology.

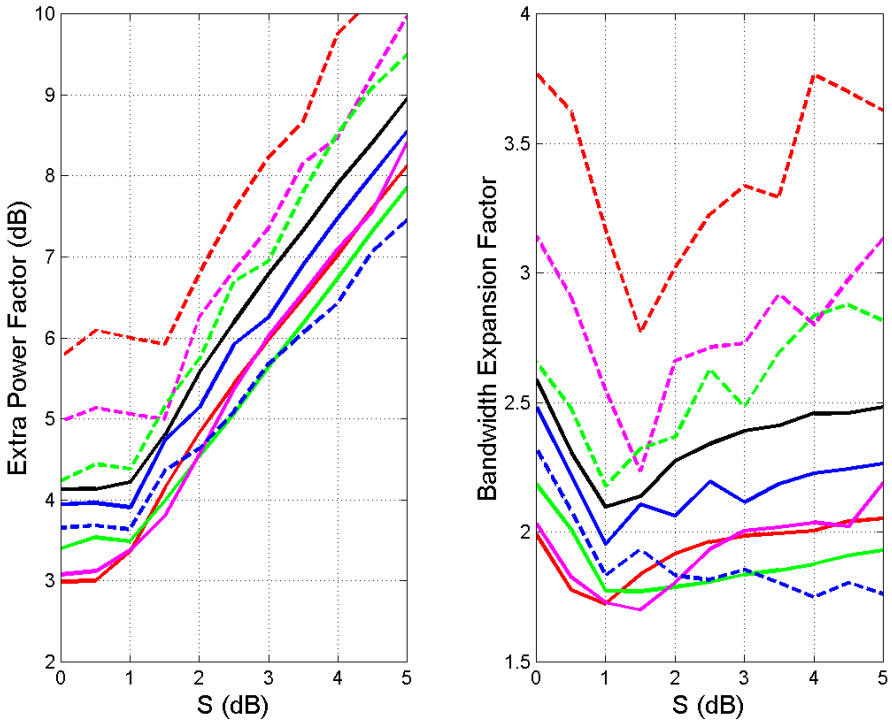

Figure 10. Left panel: Extra power factor versus the threshold S**; Right panel:** Maximum bandwidth factor versus the threshold S at the indicated sites, details of Figure 8 and 9**.** Spino d'Adda: continuous blue line; Gera Lario: continuous black line; Fucino: continuous red line; Madrid: continuous green line; Prague: continuous magenta line; Tampa: dashed red line; Norman: dashed magenta line; White Sands: dashed green line; Vancouver: dashed blue line.

 doi:10.20944/preprints202403.0017.v1

Table 5. Minimum total power margin (dB) and minimum bandwidth expansion factor at the indicated sites, from Figure 10. For example, in the Tampa geographical area the final total power margin is $1.5 + 5.9 = 7.4$ dB, with a bandwidth expansion factor ≈ 2.8, being $S = 1.5$ dB the threshold of minimum bandwidth expansion factor (Figure 10, right panel) and ~ 5.9 dB the extra power factor (Figure 10, left panel).

Site	Total power margin	Bandwidth expansion factor
Spino d'Adda (Italy)	$1.0 + 3.9 = 4.9$	1.95
Gera Lario (Italy)	$1.0 + 4.2 = 5.2$	2.10
Fucino (Italy)	$0.3 + 3.0 = 3.5$	1.75
Madrid (Spain)	$1.0 + 3.5 = 4.5$	1.80
Prague (Czech Republic)	$1.5 + 3.8 = 5.3$	1.70
Tampa (Florida)	$1.5 + 5.9 = 7.4$	2.80
Norman (Oklahoma)	$1.5 + 5.0 = 2.0$	2.25
White Sands (New Mexico)	$1.0 + 4.4 = 5.4$	2.20
Vancouver (British Columbia)	$1.0 + 3.7 = 4.7$	1.80

5. Conclusion

We have recalled that the traditional approach of considering the average probability distribution of rain attenuation is too pessimistic, in terms of power margin, in designing data transfer channels. In fact, if the data volume downloadable during rainfall is more valuable than the instantaneous symbol rate – such as in remote sensing and internet of things (IoT) using satellites – the method discussed in [10], and summarized in Section 2 of the present paper, can avoid overdesign. However, this method is usefull only if: (a) data must be downloaded also when it is raining; (b) real–time communication is not strictly required.

The method is charaterized only by a single parameter, namely the mean efficiency $0 \leq \eta \leq 1$ of the link, and it can transfer the same data volume as if the link were in clear–sky conditions.

According to theory, a small power margin and a relatively small bandwidth expansion – regardless of instantaneous rain attenuation – allow to deliver a mean symbol rate equal to the symbol rate obtainable with no rainfall.

We have applied the method to the links of GeoSurf satellite constellations [20], which have vertical (zenith) paths at any latitude. Since no measurements or predictions are available for zenith paths, we have considered as experimental results the rain attenuation time series $A(t)$ simulated at 80 GHz (mm–wave), circular polarization, with the Synthetic Storm Technique [21] from rain-rate time series $R(t)$, recorded on–site for several years.

We have found that the power margins are always small, very well within current technology. The maximum bandwidth necessary might be large if the bandwidth in clear–sky conditions is already large; therefore, this might be the most critical issue in practical applications. The evolution of spread–spectrum technology could ease its application.

We have generalized the method by supposing that a small power margin S (dB) is already available so that the method is applied only in the intervals in which the attenuation threshold S is exceeded, i.e. when $A(t) \geq S > 0$. In this case, the total power margin ranges from 2.0 dB to 7.4 dB and the bandwidth expansion factor ranges from 1.70 to 2.80. The power margin required is very small for all sites, well within the current technology; the bandwith expansion factor *per se* is not very large, but it can be a problem if the clear–sky bandwidth is already large. Future work should assess the sensitivity of the method to errors in matching the theoretical parameters to those measured or simulated with the Synthetic Storm Technique.

Funding: This research received no external funding.

Data Availability Statement: Data area available from the Author

 doi:10.20944/preprints202403.0017.v1

Acknowledgments: Carlo Riva, my colleague at Politecnico di Milano, is gratefully acknwledged fro running the SST.

Conflicts of Interest: The author declares no conflicts of interest.

Appendix A

The appendix reports examples of $A(t)$ and $\gamma(t)$, at different sites.

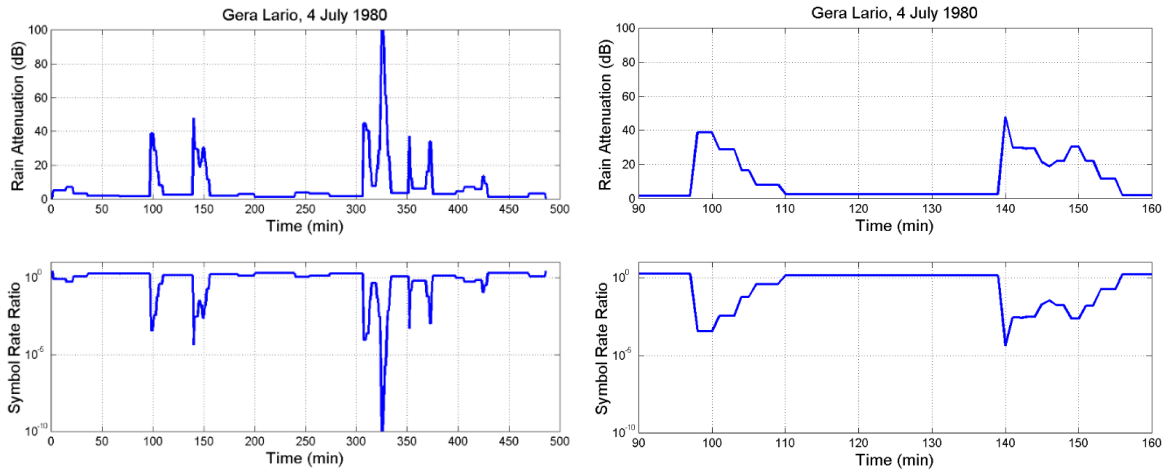

(**a**) (**b**)

Figure A1. Upper Panel: (a) Rain attenuation time series $A(t)$: (b) detail. **Lower panel**: (a) Symbol rate ratio $\gamma(t)$; (b) detail. Gera Lario.

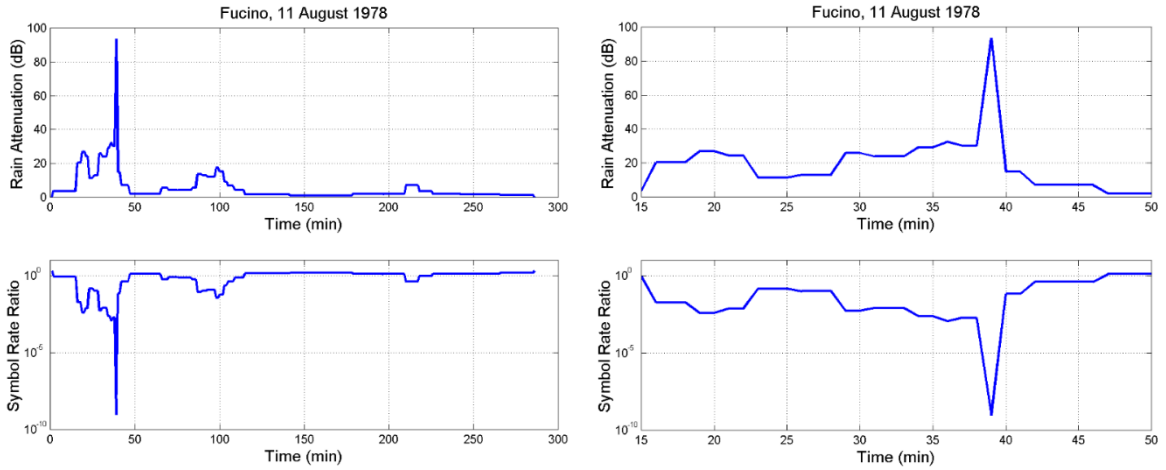

(**a**) (**b**)

Figure A2. Upper Panel: (a) Rain attenuation time series $A(t)$: (b) detail. **Lower panel**: (a) Symbol rate ratio $\gamma(t)$; (b) detail. Fucino.

Preprints.org (www.preprints.org) | NOT PEER-REVIEWED | Posted: 1 March 2024 doi:10.20944/preprints202403.0017.v1

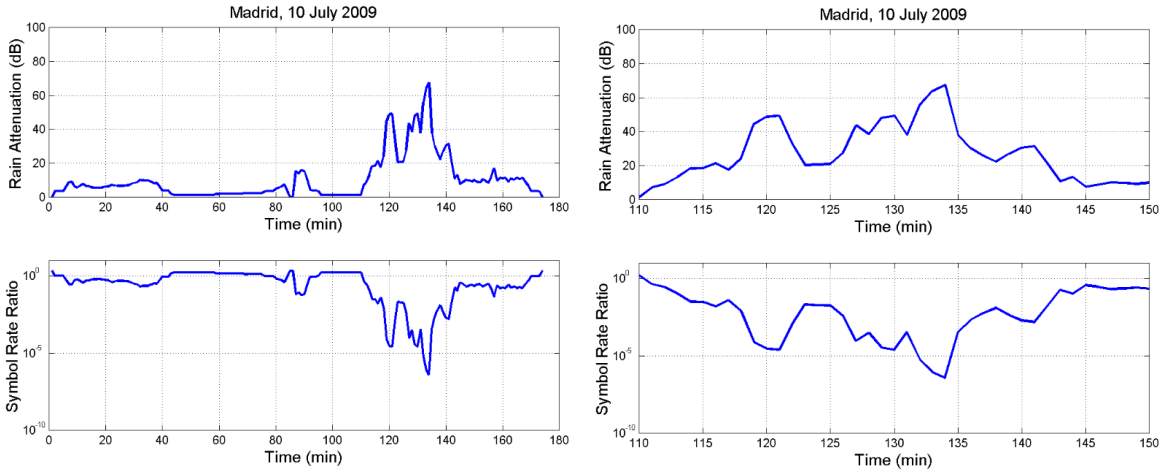

(**a**) (**b**)

Figure A3. Upper Panel: (a) Rain attenuation time series $A(t)$: (b) detail. **Lower panel**: (a) Symbol rate ratio $\gamma(t)$; (b) detail. Madrid.

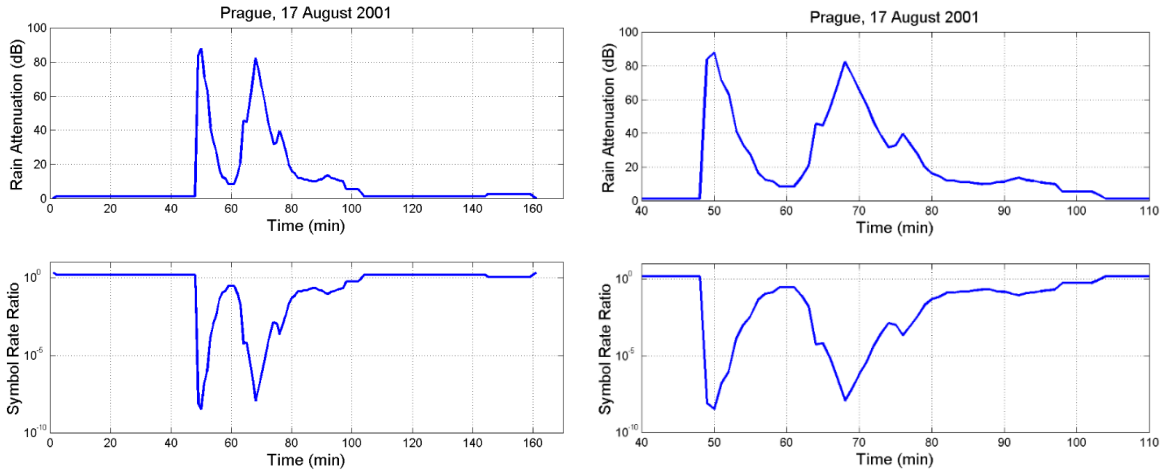

(**a**) (**b**)

Figure A4. Upper Panel: (a) Rain attenuation time series $A(t)$: (b) detail. **Lower panel**: (a) Symbol rate raio $\gamma(t)$; (b) detail. Prague.

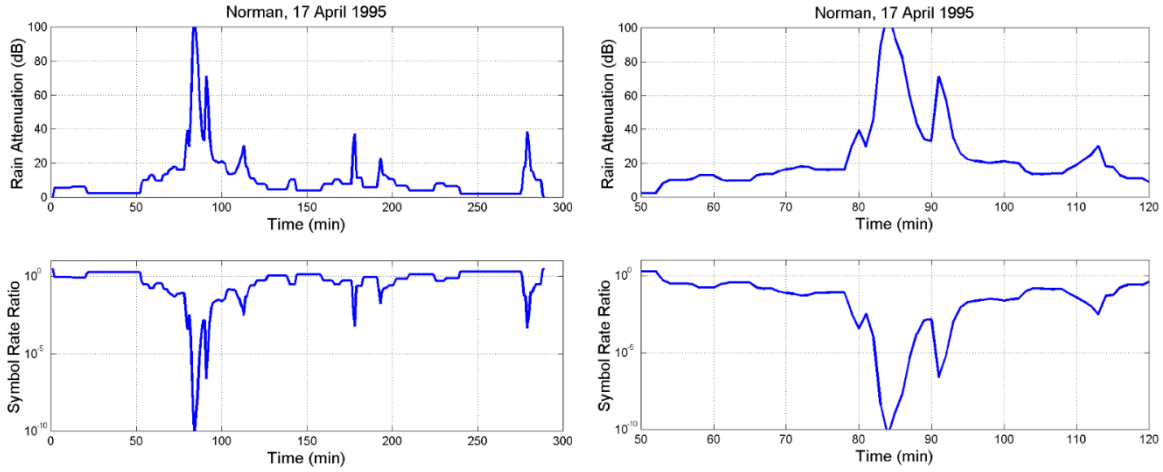

(**a**) (**b**)

Figure A5. Upper Panel: (a) Rain attenuation time series $A(t)$: (b) detail. **Lower panel**: (a) Symbol rate ratio $\gamma(t)$; (b) detail. Norman.

 doi:10.20944/preprints202403.0017.v1

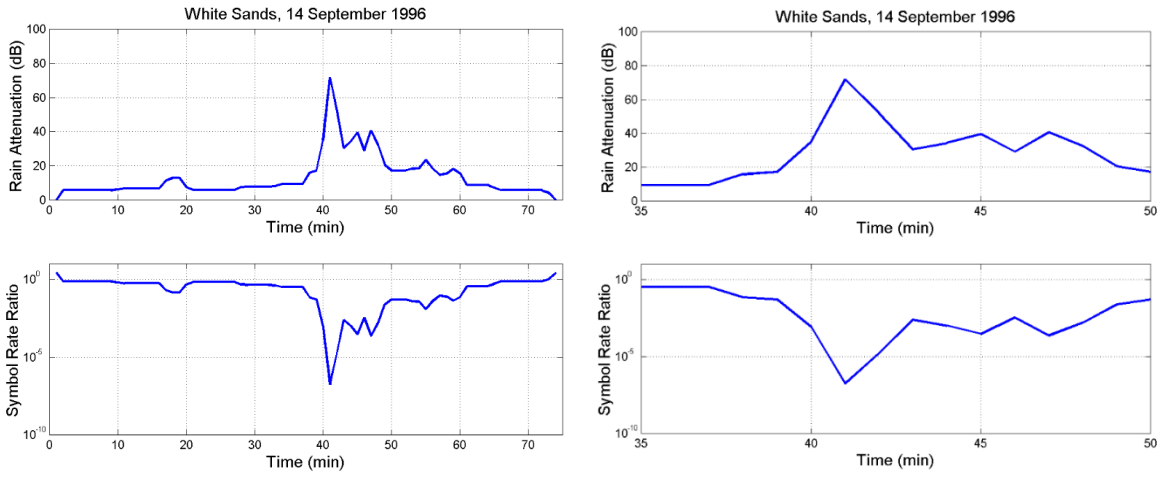

(**a**) (**b**)

Figure A6. Upper Panel: (a) Rain attenuation time series $A(t)$: (b) detail. **Lower panel**: (a) Symbol rate ratio $\gamma(t)$; (b) detail. White Sands.

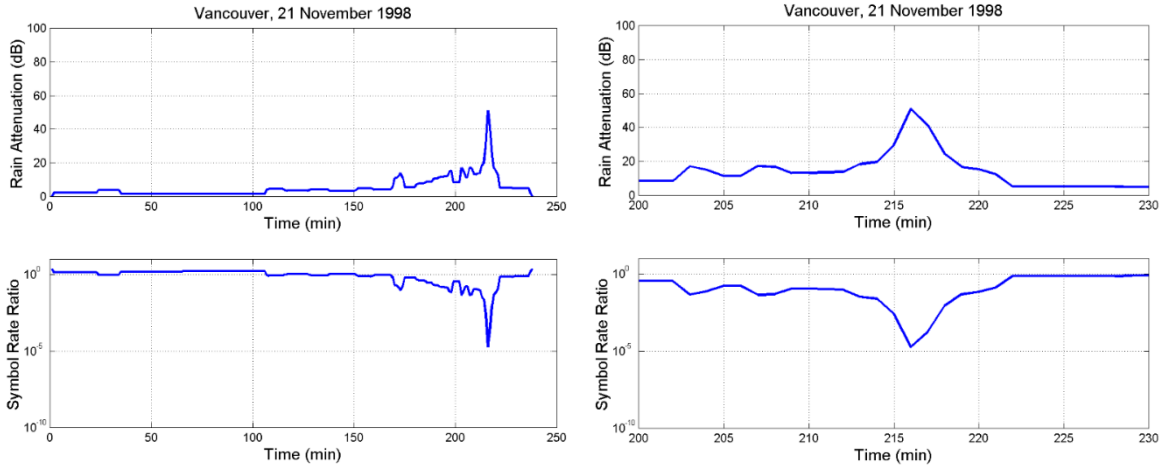

(**a**) (**b**)

Figure A7. Upper Panel: (a) Rain attenuation time series $A(t)$: (b) detail. **Lower panel**: (a) Symbol rate ratio $\gamma(t)$; (b) detail. Vancouver.

References

1. Matricciani, E., Riva, C., The search for the most reliable long–term rain attenuation cdf of a slant path and the impact on prediction models, **2005**, *IEEE Transactions on Antennas and Propagation*, 53, 3075–3079.
2. Matricciani, E.; Riva, C.; Luini, L. Tropospheric Attenuation in GeoSurf Satellite Constellations. *Remote Sens.* **2021**, *13*, 5180. https://doi.org/10.3390/rs13245180.
3. Matricciani, E.; Riva, C. Outage Probability versus Carrier Frequency in GeoSurf Satellite Constellations with Radio–Links Faded by Rain. *Telecom* **2022**, *3*, 504–513. https://doi.org/10.3390/telecom3030027.
4. Matricciani, E.; Riva, C. Transfer–functions and Linear Distortions in Ultra–Wideband Channels Faded by Rain in GeoSurf Satellite Constellations. *Future Internet* **2023**, *15*, 27. https://doi.org/10.3390/fi15010027.
5. Matricciani, E.; Magarini, M.; Riva, C. Feasibility of Ultra–Wideband Channels at Millimeter Wavelengths Faded by Rain in GeoSurf Satellite Constellations. *Telecom* **2023**, *4*, 732–745. https://doi.org/10.3390/telecom4040033.
6. Badron, K.; Ismail, A.F.; Din, J.; Tharek, A.R. Rain induced attenuation studies for V–band satellite communication in tropical region. *J. Atmos. Sol.–Terr. Phys.* **2011**, *73*, 601–610.
7. Boulanger, X.; Gabard, B.; Casadebaig, L.; Castanet, L. Four Years of Total Attenuation Statistics of Earth–Space Propagation Experiments at Ka–Band in Toulouse. *IEEE Trans. Antennas Propag.* **2015**, *63*, 2203–2214. https://doi.org/10.1109/TAP.2015.2407376.

8. Kelmendi, A.; Hrovat, A.; Mohorčič, M.; Švigelj, A. Alphasat Propagation Measurements at Ka and Q–Bands in Ljubljana: Three Years' Statistical Analysis. *IEEE Antennas Wirel. Propag. Lett.* **2021,** 20, 174–178. https://doi.org/10.1109/LAWP.2020.3043321.
9. Recommendation ITU–R P.618–14. *Propagation Data and Prediction Methods Required for the Design of Earth–Space Telecommunication Systems*; ITU: Geneva, Switzerland, 2023; Volume 8.
10. Matricciani, E., A method to achieve clear-sky data-volume download in satellite links affected by tropospheric attenuation, *Int. J. Satell. Commun. Netw.*, **2016**34:713–723.
11. Andrea J. Goldsmith, Soon-Ghee Chua, Adaptive Coded Modulation for Fading Channels, *IEEE Transactions on Communications*, **1998**, 46, 595–602.
12. E. Alberty, S. Defever, C. Moreau, R.De Gaudenzi, A. Ginesi, R. Rinaldo, g. Gallinaro, A. Vernucci, *Adaptive Coding and Modulation for the DVB-S2 Standard Interactive Applications: Capacity Assessment and Key System Issues*, IEEE Wireless Communications, August 2007, 61–69.
13. H. Bischl, H. Brandt, T. de Cola, R. De Gaudenzi, E. Eberlein, N. Girault, E. Alberty, S. Lipp, R. Rinaldo, B. Rislow, J.A. Skard, J. Tousch, G. Ulbricht, Adaptive Coding and Modulation for satellite broadband networks: From theory to practice, *International Int. J. Satell. Commun. Netw.*, **2010**, 28, 59–111.
14. Zhang, S.; Yu, G.; Yu, S.; Zhang, Y.; Zhang, Y. Weather-Conscious Adaptive Modulation and Coding Scheme for Satellite-Related Ubiquitous Networking and Computing. *Electronics* **2022**, *11*, 1297. https://doi.org/10.3390/electronics11091297.
15. Wang, Z.; Lu, F.; Wang, D.; Zhang, X.; Li, J.; Li, J. A Transmission Efficiency Evaluation Method of Adaptive Coding Modulation for Ka-Band Data-Transmission of LEO EO Satellites. *Sensors* **2022**, *22*, 5423. https://doi.org/10.3390/s22145423.
16. Mhangara, P.; Mapurisa, W. Multi-mission earth observation data processing system. *Sensors* **2019**, *19*, 3831.
17. Yang, X.Q.; Li, L.; Jin, F.; Zhang, J.P. Research on satellite-borne high-speed adaptive transmission technique. *Space Electron. Technol.* **2014**, *11*, 20–24.
18. Zhang, J.P. Adaptive coding and modulation for remote sensing satellite. *Space Electron. Technol.* **2016**, *13*, 78–86.
19. Wang, Z.G.; Wang, D.B.; Hu, Y.; Lu, F. Analysis on application efficiency of adaptive coding and modulation for LEO remote sensing satellite at Ka-band. *Spacecr. Eng.* **2021**, *30*, 69–76.
20. Matricciani, E. Geocentric Spherical Surfaces Emulating the Geostationary Orbit at Any Latitude with Zenith Links. *Future Internet* **2020**, *12*, 16. https://doi.org/10.3390/fi12010016.
21. Matricciani, E. Physical–mathematical model of the dynamics of rain attenuation based on rain rate time series and a two–layer vertical structure of precipitation. *Radio Sci.* **1996**, *31*, 281–295. https://doi.org/10.1029/95rs03129.
22. Matricciani, E. Prediction of fade duration due to rain in satellite communication systems. *Radio Sci.* **1997**, *22*, 935–941.
23. Chakraborty, S.; Verma, P.; Paudel, B.; Shukla, A.; Das, S. Validation of Synthetic Storm Technique for Rain Attenuation Prediction Over High–Rainfall Tropical Region. *IEEE Geosci. Remote Sens. Lett.* **2021**, *19*, 1–4. https://doi.org/10.1109/LGRS.2021.3068334.
24. Jong, S.L.; Riva, C.; D'Amico, M.; Lam, H.Y.; Yunus, M.M.; Din, J. Performance of synthetic storm technique in estimating fade dynamics in equatorial Malaysia. *Int. J. Satell. Commun. Netw.* **2018**, 36, 416–426. https://doi.org/10.1002/sat.1246.
25. E. Matricciani, Probability distributions of rain attenuation obtainable with linear combining techniques in space-to-Earth links using time diversity, *International Journal of Satellite Communications and Networking*, 2017, DOI: 10.1002/sat.1214, 2017;1–18.
26. E. Matricciani, Physical-mathematical model of dynamics of rain attenuation with application to power spectrum, *Electronics Letters*, 1994, 30, 522-524.
27. Nandi, D.D.; Pérez-Fontán, F.; Pastoriza-Santos, V.; Machado, F. Application of synthetic storm technique for rain attenuation prediction at Ka and Q band for a temperate Location, Vigo, Spain. *Adv. Space Res.* **2020**, *66*, 800–809.
28. Matricciani, E.; Riva, C. Duration of Rainfall Fades in GeoSurf Satellite Constellations. *Appl. Sci.* **2024**, *14*, 1865. https://doi.org/10.3390/app14051865.
29. Marzano, F.S., Modeling antenna noise temperature due to rain clouds at microwave and millimeter–wave frequencies, **2006**, *IEEE Transactions on Antennas and Propagation*, 54, 1305–1317.

30. Turin, G.L. Introduction to spread spectrum antimultipath techniques and their application to urban digital radio. *Proc. IEEE* **1980**, *68*, 328–353.
31. Pickholtz, R.; Schilling, D.; Milstein, L. Theory of spread–spectrum communications—A tutorial. *IEEE Trans. Commun.* **1982**, *30*, 855–884.
32. Viterbi, A.J. *CDMA Principles of Spread Spectrum Communications*; Addinson–Wesly: Reading, MA, USA, 1995.
33. Dinan, E.H.; Jabbari, B. Spreading codes for direct sequence CDMA and wideband CDMA celluar networks. *IEEE Commun. Mag.* **1998**, *36*, 48–54.
34. Veeravalli, V.V.; Mantravadi, A. The coding–spreading trade–off in CDMA systems. *IEEE Trans. Sel. Areas Commun.* **2002**, *20*, 396–408.
35. E. Matricciani, Rate of change of signal attenuation from SIRIO at 11.6 GHz, *Electronics Letters*, 1981, 17, 139-141.
36. Garcia–Rubia, J.M.; Riera, J.M.; Garcia–del–Pino, P.; Pimienta–del–Valle, D.; Siles, G.A. Fade and Interfade Duration Characteristics in a Slant–Path *Ka*–Band Link. *IEEE Trans. Antennas Propag.* **2017**, 65, 7198–7206. https://doi.org/10.1109/TAP.2017.2758839.
37. Chakraborty, S.; Chakraborty, M.; Das, S. Second order experimental statistics of rain attenuation at Ka band in a tropical location. Adv. Space Res. **2012**, *67*, 4043–4053, https://doi.org/10.1016/j.asr.2021.02.033.
38. Papafragkakis, A.Z.; Kourogiorgas, C.I.; Panagopoulos, A.D.; Ventouras, S. Second Order Excess Attenuation Statistics in Athens, Greece at 19.701 GHz using ALPHASAT. In Proceedings of the 12th International Symposium on Communication Systems, Networks and Digital Signal Processing (CSNDSP), Porto, Portugal, 20–22 July 2020. https://doi.org/10.1109/CSNDSP49049.2020.9249506.
39. Das, S.; Chakraborty, M.; Chakraborty, S.; Shukla, A.; Acharya, R. Experimental studies of Ka Band Rain Fade Slope at a Tropical Location of India. *Adv. Space Res.* **2020**, *66*, 1551–1557.
40. Jong, S.L.; Riva, C.; Din, J.; D'Amico, M.; Lam, H.Y. Fade slope analysis for *Ku*-band earth-space communication links in Malaysia. *IET Microw. Antennas Propag.* **2019**, *13*, 2330–2335.
41. Samad, M.A.; Diba, F.D.; Choi, D.-Y. A Survey of Rain Fade Models for Earth–Space Telecommunication Links—Taxonomy, Methods, and Comparative Study. *Remote Sens.* **2021**, *13*, 1965. https://doi.org/10.3390/rs13101965.